IEEE Access
Multidisciplinary ⋮ Rapid Review ⋮ Open Access Journal

Received 8 October 2023, accepted 8 November 2023, date of publication 14 November 2023,
date of current version 22 November 2023.

*Digital Object Identifier 10.1109/ACCESS.2023.3332633*

RESEARCH ARTICLE

# Fault Location of the Renewable Energy Sources Connected Distribution Networks Based on Time Differences of the Modal Traveling Waves

**XIAOFENG REN[1,2], YIHANG PAN[1], MENG HOU[1], RUI LIANG[1], (Senior Member, IEEE), LINGDONG SU[2], QUANJIN WANG[3], AND PENG ZHANG[1], (Graduate Student Member, IEEE)**

[1]School of Electrical Engineering, China University of Mining and Technology, Xuzhou 221116, China
[2]State Grid Xuzhou Power Supply Company, Xuzhou 221005, China
[3]State Grid Linyi Power Supply Company, Linyi 276000, China

Corresponding author: Rui Liang (liangrui@cumt.edu.cn)

This work was supported in part by the National Natural Science Foundation of China under Grant 52077215, and in part by the State Grid Xuzhou Power Supply Company Science and Technology Program under Grant SGJSXZ00KJJS2311869.

**ABSTRACT** The topology of the distribution network and direction of the power flow will change when distributed generators (DGs) are connected to it, making it difficult to locate faults using conventional techniques like the impedance approach. Aiming at the two-phase short-circuit grounding faults of active distribution networks, this paper proposes a fault location method based on the time difference of the traveling wave modulus. The first step is the proposal of a zero-mode time-of-arrival calibration method for the ideal frequency band through the analysis of the attenuation of zero-mode traveling wave transmission. Next, define the relative wave velocity, research the quantitative relationship between the modulus transmission time difference and the zero-mode and aerial-mode wave velocities, and establish equation constraints between the modulus transmission time difference, relative wave velocity, and transmission distance. Then, time bounds and dynamic inequality constraints that establish relative wave velocities by fitting. Finally, combined with the abnormal data processing strategy, with the goal of minimizing the weighted deviation of the modulus time difference, the particle swarm optimization (PSO) algorithm is used to solve the fault distance. The PSCAD simulation result demonstrates that the method proposed in this paper has the advantages of high accuracy, strong error tolerance, and strong adaptability, and can quickly and accurately locate faults.

**INDEX TERMS** Fault location, traveling wave modulus time difference, renewable energy sources, weighted deviation, preferred frequency band.

## I. INTRODUCTION

Safe and reliable operation of distribution networks is an important guarantee for people's production and lives. Rapid and accurate localization of the fault promotes the speedy removal of the fault line. Improving the efficiency of fault management and the dependability of power grid operation after faults occur has significant social and economic benefits [1]. The current of two-phase short-circuit grounding faults and the variations in phase voltage of the busbar to ground are greatly affected by the grounding location and fault resistance. Conventional protection is difficult to accurately locate and remove faults, leading to the long-term existence of faults and seriously threatening the safety of the power grid [2], [3]. Even though a two-phase short-circuit grounding fault has a lower likelihood than a single-phase grounding fault, it causes much more damage to the power system. According to the detected current information, the impact of incomplete and error information is excluded after judgment two times by the adaptive matrix algorithm, then to determine the fault [4]. In [5], an extended fault-location formulation for a general distribution system was proposed. The method

The associate editor coordinating the review of this manuscript and approving it for publication was Barbara Guidi.

is based on apparent fault impedance calculation and can calculate sufficiently accurate fault location in a distribution system with intermediate taps, lateral and with heterogeneous lines. Although the prospect is broad, these algorithms mainly aim at the single-phase ground faults [6]. With the advent of widespread access to distributed power on a large scale, the operation regulation and fault characteristics of the distribution network are poised to undergo profound transformations [7], [8], including the emergence of two-way power flow and dynamic changes in network topology [9]. As one delves deeper into the intricacies of the fault mechanism, the complexity of the analysis increases manifold. The characteristics of distribution network grounding faults with neutral points grounded through arc suppression coils, in particular, may be weakened, making fault location more difficult. It is worth noting that conventional fault location techniques, such as the impedance method, may be inadequate in such circumstances [10].

Compared with single-phase grounding faults, the fault characteristics of two-phase short-circuit grounding faults in renewable energy sources connected distribution networks are more obvious, and traveling wave characteristics are more suitable for fault location. The traveling wave method has been widely used in the field of transmission network fault location due to its high accuracy and reliability. At present, the traveling wave method can be categorized into three sub-types: single-ended methods [11], double-ended methods [12] and wide-area methods [13], [14].

References [15] and [16] utilize the traveling wave information at multiple opposite-end buses to perform the extended double-ended traveling wave methods, and take the average of the calculation results as the fault distance. According to the correlation analysis of the initial arrival time of traveling waves, an effective fault section identification method was developed in [17]. This approach combines the transmission path of the initial traveling wave and fuses and processes waveform data from the entire network to accurately locate faults. Reference [18] establishes the arrival time difference matrix of traveling waves, and uses the matrix difference before and after the fault to locate the fault.

The structure of the distribution network is complex since there are many branches. When the topology of the distribution network is known, a traveling wave location system based on the entire distribution network can be established according to the wide-area traveling waves [19], [20], but there are still microsecond-level errors, which limits the improvement of fault location accuracy. A technique proposed in [21] merges the virtual fault point into the network topology after each reset and recalculates the shortest distance between the node and other nodes. This method is simple and effective, but the calculation burden is heavy. The access of distributed generators makes the distribution network fault form more complicated, especially the grounding fault characteristics of the distribution network, whose neutral point grounded through the arc suppression coil is further weakened, and the grounding fault location becomes more difficult [22]. In response to the shortcomings of standard intelligent algorithms in high-dimensional large-scale distributed power grid location selection, [23] proposes a hybrid algorithm combining improved matrix algorithm to solve the location of fault sections. Although the traveling wave method has high location accuracy and widespread practice, it still faces the problems such as difficult identification of the traveling wave head, and great influence from traveling wave speed in distribution networks. At the same time, the probability of abnormal data also increases with the growth of traveling wave data. In [19], the researchers establish overdetermined equations based on the law of traveling wave transmission, weaken the influence of abnormal data through redundant equations, and use the wide-area traveling wave method for fault location. This method utilizes redundant information to identify and eliminates the impact of abnormal data, thereby improving fault location accuracy to a certain extent. However, the above methods focus on abnormal data with high order of magnitude, without considering the abnormal data caused by synchronization and sampling errors.

Aiming at the above problems, this paper proposes a two-phase grounding fault location method based on modulus time difference for new energy distribution networks. By analyzing the time-frequency characteristics of the zero-mode wave head, the accurate zero-mode wave head calibration method is condensed, and the relationship among the modulus time difference, the wave speed and distance is studied. The relative wave speed is defined, its dynamic fluctuation range is obtained through the simulation data, and the simulation model is finally established to verify the effectiveness and accuracy of the proposed method. The main contributions of this paper are expressed as follows:

(1) The stability of the arrival time for the traveling wave zero mode component is significantly lower than that of the aerial mode component, which poses a challenge when introducing zero mode components for fault location. This article uses the S-transform to extract the time-frequency characteristics of the traveling wave zero mode component to analyze the cause of its instability, and establishes a calibration method for zero mode wave head arrival time based on this analysis.

(2) In weak synchronous or asynchronous situations, the traveling waves between nodes are recorded by different time benchmarks. The difference in the arrival time of the wave heads between the two nodes cannot match the distance difference between the fault point and different nodes. Based on differences in wave velocity between zero mode and aerial mode, this article constructs a transmission relationship between them. Considering wave velocity and arrival time error, a fault location model is established with the weighted deviation degree of modals time difference as the target, and the fault location is achieved by comprehensively using zero mode and aerial mode traveling wave information under different time benchmarks.

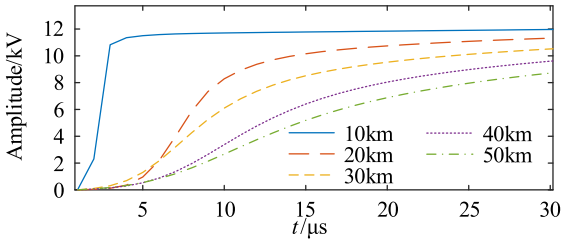


**FIGURE 1.** Comparison of wave head morphology at different distances.

(3) The existing methods mainly focus on abnormal data with high orders of magnitude, without considering the impact of error data caused by synchronization and sampling errors. This article proposes a strategy for identifying and processing abnormal data based on contradictory constraints, which avoids the degradation location accuracy due to the pollution from such data.

## II. ANALYSIS OF THE PROPAGATION FEATURES OF THE TRAVELING WAVES

### A. FREQUENCY-DEPENDENT CHARACTERISTICS

#### 1) FREQUENCY-DEPENDENT ATTENUATION CHARACTERISTICS

The fault traveling wave propagates on the line in a transient form after the fault occurs. The energy loss caused by line resistance and insulation leakage conductance makes the amplitude of the traveling wave head attenuate during the transmission process. The skin effect is more significant in transmission, and the equivalent line resistance is higher due to the traveling wave mutation's abundance of high-frequency components, which causes a slower steepness of wave head [24]. Fig.1 shows a shape comparison of the wave head after the same traveling wave transmitted different distances.

The wave head of a traveling wave can be regarded as the superposition of multiple frequency components, which can be expressed by

$$\begin{cases} A_{tw} = \sum (e^{-\gamma(\omega)x} f_\omega(t)) \\ \gamma(\omega) = \sqrt{(R + j\omega L)(G + j\omega C)} = \alpha(\omega) + j\beta(\omega) \end{cases} \quad (1)$$

where $A_{tw}$ is the amplitude of the traveling wave head, $f_\omega(t)$ is the amplitude of the wave head of the frequency $\omega$. $R$, $L$, $G$, and $C$ are the resistance, inductance, conductance, and capacitance of lines, respectively. $\alpha(\omega)$ and $\beta(\omega)$ are the attenuation coefficient and phase coefficient of the traveling wave at different frequencies, respectively. The amplitude attenuation of each frequency component in the traveling wave signal is different. Both $\alpha(\omega)$ and $\beta(\omega)$ increase with the growth of frequency from equation (1) as the propagation distance increases. The higher the frequency, the more significant the amplitude attenuation of the component.

By setting nine measuring points on a line and using the wavelet transform to collect wave heads in different frequency bands, the attenuation trend is obtained as shown in Fig.2. The waveforms of different colors represent

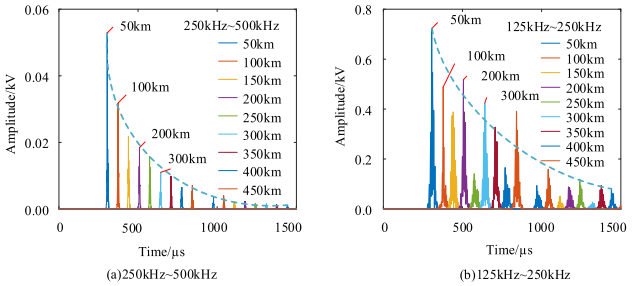


**FIGURE 2.** Time-frequency distribution of aerial mode traveling waves and Arrival time of different.

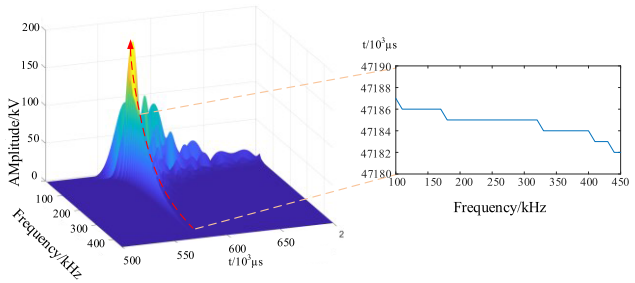


**FIGURE 3.** Comparison of amplitude attenuation in different frequency bands of wave heads.

the absolute values of the wavelet frequency components extracted by the wavelet transform at different distances. It can be seen that the high frequency components attenuate faster than the low ones due to the different parameters of the different frequency components during the transmission process. This is the frequency-dependent attenuation characteristic of the traveling wave.

#### 2) FREQUENCY-DEPENDENT ATTENUATION CHARACTERISTICS

Different frequency components of traveling waves not only have different amplitude attenuation characteristics but also exhibit different propagation speeds. At a distance of 10 km from the fault point, the aerial mode traveling wave is measured with a sampling rate of 1 MHz, and the spectrum diagram drawn by S-transformation is shown in Fig.3.

Taking the modulus maximum value of each frequency component as the arrival time of the frequency, the result of 100 kHz–450 kHz is shown in Fig.3. It can be seen that the arrival time increases with the decrease in frequency, which means that the wave velocity of the low-frequency component is slower than that of the high-frequency component. The velocity of traveling waves is closely related to frequency and line parameters, and the velocities of different frequency components are different, and the high-frequency components have a faster transmission speed [25].

The high-frequency component with the fastest transmission in the wave head is detected first. However, since the high-frequency component attenuates quickly, the traveling wave acquisition device is limited by its resolution and cannot identify the highest frequency component after the

attenuation reaches a certain level, so it can only detect the sub-high frequency components. The traveling wave velocity at this time is actually the wave velocity of the sub-high frequency component. As the transmission distance increases, the attenuation becomes more and more significant, the frequency component of the traveling wave becomes lower and lower, and the corresponding wave velocity becomes slower [26].

### B. ANALYSIS OF TRAVELING WAVE CHARACTERISTICS IN THE DISTRIBUTION NETWORK WITH DGS

#### 1) EFFECTS OF DISTRIBUTED GENERATORS AND POWER ELECTRONIC EQUIPMENT ON THE INITIAL TRAVELING WAVE HEAD

The power electronics equipment will reduce the switching frequency as much as possible to reduce the switching loss. The switching frequency of the converter in the distributed generators is usually 2 kHz. Hence, the harmonics generated by the switch are mainly at 2 kHz. Selecting a suitable frequency band signal can avoid the influence of the harmonics generated by the power electronic equipment on the initial fault wave head to a certain extent. In addition, the detection of the initial traveling wave is that the wave head rise or fall time is less than 10 $\mu$s. Regardless of the harmonic situation generated by the power electronic equipment, the LCL filter filters the output signal of the thyristor or the PWM signal of the IGBT before flowing into the alternating current side, and the wave head rising or falling time is generally greater than 1ms.

Since the transmission speed of the fault traveling wave is close to the that of light, and the distribution lines are generally short, the initial fault traveling wave head can be detected at the microsecond level if the terminal transformer of each branch is equipped with a traveling wave acquisition device. The response delay of the power electronic equipment control system is around milliseconds, and the initial fault traveling wave head has reached the detection device before the control system acts. At the same time, the generation mechanism of traveling waves follows the wave process theory. The transmission of the initial traveling wave head is only related to the fault conditions and the distributed parameters of the line. It is not affected by the power supply (grid-connected inverter, control system) or the backside system of the fault point. The grid-connected inverter and filter can be regarded as the boundary of the line, which will affect the subsequent refraction and reflection of the traveling wave, while the wave head of the initial traveling wave is basically not affected. In addition, when distributed power is connected to the grid, the node voltage is affected by the DG access position and capacity. The slight fluctuations on the node voltage caused by DG can be negligible.

#### 2) COMPARISON OF TRAVELING WAVE SIGNALS IN DISTRIBUTION AND TRANSMISSION NETWORKS

Taking the 10 kV distribution system as an example, compared with the transmission line, there is a certain difference in the fault traveling wave signal of the distribution network. The main influencing factors are analyzed in detail as follows.

The structure of the distribution network is complex, and there are many branches. The fault traveling wave will be refracted and reflected at the branch nodes and the connection of the cable overhead line. Equation (2) is the voltage refraction coefficient, $Z_{1c}$ is the wave impedance of the incident wave branch, $Z_{2c}$ is the parallel impedance of all branch wave impedances directly connected to the branch node except the incident wave branch. Assuming the total number of branches is n, the fault traveling wave attenuates to $2/n$ of the initial traveling wave after passing the branch node. Line parameters also affect the attenuation of the fault traveling wave. Equations (3) and (4) are the expressions of the transmission coefficient and the transfer function. The transfer function is related to the traveling wave transmission distance, frequency, and line parameters. For the same transmission distance, the attenuation of distribution overhead lines is slightly greater than that of overhead lines, and the attenuation of cables is much greater than that of overhead lines.

$$r_f = \frac{2Z_{2c}}{Z_{2c} + Z_{1c}} \tag{2}$$

$$\begin{aligned}\gamma(\omega) &= \sqrt{Z_0 Y_0} = \sqrt{(R_0 + j\omega L_0)(G_0 + j\omega C_0)} \\ &= \alpha(\omega) + j\beta(\omega)\end{aligned} \tag{3}$$

$$A(\omega) = e^{-rx} \tag{4}$$

The voltage traveling waves are detected by voltage traveling wave transducers, which are connected to the ground wire of the capacitive equipment (transformers). It detects the change and characteristics of the current on the ground wire of the equipment by detecting the change of the induced electromotive force, thereby reflecting the sudden signal of the line voltage traveling wave.

The equivalent capacitance of the distribution transformer is smaller than that of the transmission network capacitive voltage transformer (CVT). Due to the difference in the equivalent capacitance, the initial traveling wave head of the distribution network fault is much smaller than that of the transmission network fault [27].

## III. FAULT LOCATION METHOD BY MODAL TRAVELING WAVES

### A. TRAVELING WAVE ARRIVAL TIME CALIBRATION

The zero-mode traveling wave transmission circuit is formed by the ground, and the aerial-mode traveling wave transmission circuit is formed by wires. Since the impedance of the ground is larger than that of the line, the attenuation during the transmission of the traveling wave zero-mode component is more obvious [28].

Since the attenuation coefficient for the zero-mode traveling wave transmission path is higher, more of its energy is concentrated in the low-frequency band, and the attenuation in the high-frequency band is significant. The time-frequency information of the zero-mode traveling wave

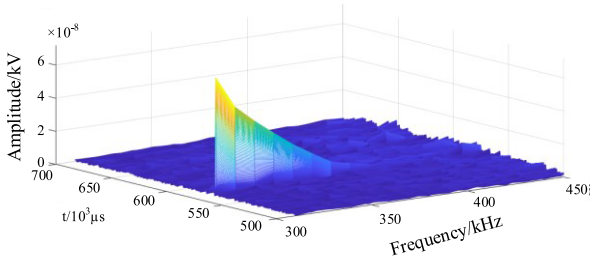


**FIGURE 4.** Detailed time-frequency distribution of zero-mode traveling waves in 300-400kHz.

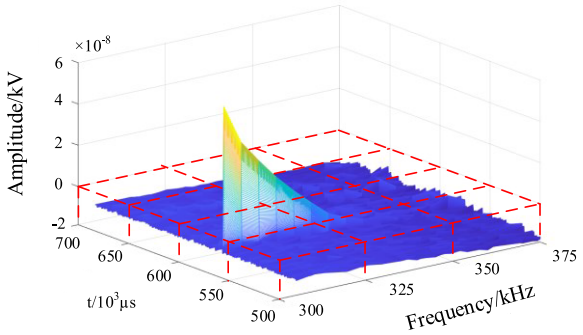


**FIGURE 5.** Detailed time-frequency distribution after difference operation.

in the 300∼400 kHz frequency band is shown in Fig.4. Due to the significant attenuation of the zero-mode traveling wave at a long distance, the frequency components at above 380 kHz have been submerged in the noise.

That noise exists on the full-time scale means there is always background noise in the spectrum obtained by S-transform, and the background noise at the same frequency is basically unchanged in order of magnitude. Thus, a zero-mode effective frequency band extraction method is formed, and the wave head is calibrated according to the effective frequency band information.

The time-frequency matrix $\boldsymbol{W}$ is obtained after S transformation of the detected zero-mode signal:

$$\boldsymbol{W} = \left[w_{ij}\right]_{\text{tmax}\times\text{fmax}} (1 \le i \le \text{tmax}, 0 \le j \le \text{fmax}) \quad (5)$$

where $w_{ij}$ is the amplitude of the traveling wave signal corresponding to frequency band $i$ at time $j$, tmax and fmax represent the upper limit of time and frequency, respectively.

Further average the rows of $\boldsymbol{W}$ to form the average time-frequency background noise matrix $\boldsymbol{W}_{\text{bn}}$:

$$\boldsymbol{W}_{\text{bn}} = \begin{pmatrix} \overline{w_1} & \cdots & \overline{w_1} \\ \vdots & \ddots & \vdots \\ \overline{w_i} & \cdots & \overline{w_i} \end{pmatrix} \quad (6)$$

The value of $\overline{w_i}$ in (6) is:

$$\overline{w_i} = \frac{\eta}{\text{tmax}} \sum_j w_{ij} (1 \le j \le \text{tmax}) \quad (7)$$

where $\eta$ is the background amplification factor, and 10 is used in this paper to ensure negative noise. Then, the negative noise is calculated by the matrix difference:

$$\boldsymbol{W}^* = \boldsymbol{W} - \boldsymbol{W}_{\text{bn}} \quad (8)$$

The matrix $\boldsymbol{W}^*$ is the zero-mode time-frequency matrix after the background noise is negatively valued. After the above processing, the negative value of the noise can be ensured, and the effective frequency band can be identified. $\boldsymbol{W}^*$ at this time is shown in Fig.5.

As shown in Fig.5, the high-frequency component of the traveling wave is negatively valued with the differential operation, and the effective frequency bands of zero mode and the flooded frequency band are distinguished in numerical signs. In consideration of the calibration's practicability and effectiveness and with the goal of acquiring as much node time information as possible, the calibration frequency band is set as 100∼200 kHz. If a node has a negative value between 100 kHz and 200 kHz, it is labeled as a fuzzy node, and the calibration frequency range is lowered to the highest frequency corresponding to the non-negative value between 100 kHz and the non-negative value; if all negative values are in the 100∼200 kHz frequency band, the node is marked as an invalid node. After each frequency band within the selected effective frequency band has been calibrated, the average value of the calibration results is taken as the final calibration result.

### B. FAULT LOCATION ALGORITHM

When an asymmetric fault occurs anywhere in the distribution network, the traveling waves of zero mode and aerial mode will be generated. Due to the different transmission paths and parameters, the zero-mode transmission speed $v_i^0$ is usually slower than the aerial-mode speed $v_i^l$. The time difference $\Delta t_i^{0l}$ between the zero-mode and aerial-mode wave head arrival times at node $i$ should conform to the following relationship:

$$\Delta t_i^{0l} = t_i^0 - t_i^l = \frac{l_{fi}}{v_i^0} - \frac{l_{fi}}{v_i^l} = \left(\frac{1}{v_i^0} - \frac{1}{v_i^l}\right) l_{fi} \quad (9)$$

where $t_i^l$ is the calibration time of the aerial-mode wave head at node $i$, $v_i^0$ and $v_i^l$ are the average wave speeds of the zero-mode and aerial-mode traveling waves transmitted to node $i$, respectively.

Define the relative velocity $v_i^{0l}$ of the zero-mode and aerial-mode of node $i$:

$$v_i^{0l} = \left(\frac{v_i^0 v_i^l}{v_i^l - v_i^0}\right) \quad (10)$$

Substituting (9) into equation (10), we have:

$$v_i^{0l} \cdot \Delta t_i^{0l} = l_{fi} \quad (11)$$

It can be seen from equation (11) that the fault distance is proportional to the modulus arrival time difference. By vectorizing the above equations to establish the shortest distance

function vector $L_f$, the relative wave velocity vector $\boldsymbol{V}^{0l}$, and the modulus time difference vector $\Delta \boldsymbol{T}^{0l}$ are:

$$\begin{cases} \boldsymbol{L}_f = \left[l_{fi}(x_f)\right]_{1\times N}(1 \le i \le N) \\ \boldsymbol{V}^{0l} = [v_i^{0l}]_{1\times N}(1 \le i \le N) \\ \Delta \boldsymbol{T}^{0l} = [\Delta t_i^{0l}]_{1\times N}(1 \le i \le N) \end{cases} \tag{12}$$

If node $i$ is not equipped with a measuring device, the corresponding element of the vector will be set to zero. The equality constraints are as follows:

$$\boldsymbol{V}^{0l*}\left(\Delta \boldsymbol{T}^{0l*}\right)^{\boldsymbol{T}} = \boldsymbol{L}_f \tag{13}$$

where $*$ represents the variable form of that vector.

According to the collected data and combined experience [29], the zero-mode wave velocity range is known to be:

$$0.8c \le v_i^0 \le 0.987c \tag{14}$$

where $c$ represents the speed of light, whose value is $3 \times 10^8$m/s.

Since the zero-mode wave velocity is slower than the aerial-mode wave velocity, the denominator of (10) is always greater than 0, so the zero-mode wave velocity is positively correlated with the relative wave velocity and the aerial-mode wave velocity is negatively correlated with the relative wave velocity. When calculating the upper limit, the wave velocity difference between the aerial mode and the zero mode at the initial moment of the fault is the smallest. The maximum value is approximately infinite, and the lower limit calculation result retains two decimal places. The fluctuation range of $v_i^{0l}$ is:

$$4.22c \le v_i^{0l} \le \infty \tag{15}$$

Fixed wave velocity constraints are difficult to adapt to changing relative wave velocities, and it is necessary to establish wave velocity constraints that vary with distance. A linear function, a quadratic function, a cubic function, and a power function are used to fit the simulated scattered point data and accurately describe how the modulus time difference changes with fault distance. The fitting curve is depicted in Fig.6.

As shown in Fig.6, the cubic function has the highest degree of fitting reliability, so it is chosen for fitting. Considering the line parameters, the wave velocity attenuation difference caused by the transmission path, and the fitting error, the relative wave velocity fluctuates within ±10% under normal circumstances. Therefore, the matrixed relative velocity constraints can be expressed as:

$$\begin{aligned} |\boldsymbol{V}^{0l} - \boldsymbol{V}^{0l*}| &\le \frac{\varepsilon \times \boldsymbol{L}_f(x)}{\Delta \boldsymbol{T}^{0l}(x)} \\ \frac{(1-\varepsilon)\times \boldsymbol{L}_f}{\Delta \boldsymbol{T}^{0l}} \le \boldsymbol{V}^{0l*} &\le \frac{(1+\varepsilon)\times \boldsymbol{L}_f}{\Delta \boldsymbol{T}^{0l}} \end{aligned} \tag{16}$$

where $\varepsilon$ is the confidence range of the relative wave velocity, which is taken as 10 in this paper.

Considering the error range and a certain margin, this paper extracts the information of the first wave head $f_s/4$–$f_s/2$ ($f_s$ is the sampling rate) frequency band by db6 wavelet transform,

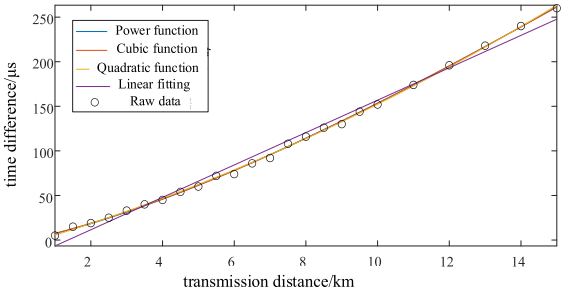


**FIGURE 6.** Fitting curve of the relationship between modulus time difference and transmission distance.

and sets the fluctuation range of the actual wave head arrival time as the range of the transient process of the frequency band, as shown in (17).

$$t_{si} < t_i < t_{ei} \tag{17}$$

where $t_i$ is the time when the first wave head reaches node $i$. $t_i$ is 0 if there is no measuring device at node $i$. $t_{ei}$ and $t_{si}$ are the transient end and starting time of the first wave head.

The arrival time of the zero-mode in different frequency domains is quite different, and the analysis of the time error of the aerial mode wave head is not applicable to the zero-mode. In this paper, the 100∼200 kHz frequency is used to calibrate the traveling wave head, and the final calibration time should be within the time fluctuation range of the subdivided frequency bands under this frequency band.

The error caused by sampling usually does not exceed one sampling period. After taking it into account, the fluctuation range of the arrival time of the zero mode is:

$$t_{i\_\min}^0 - \frac{1}{f_s} \le t_i^0 \le t_{i\_\max}^0 + \frac{1}{f_s} \tag{18}$$

where $t_{i\_\max}^0$ and $t_{i\_\min}^0$ are the maximum and minimum arrival times of zero-mode at node $i$, respectively.

Combining the time error range of the aerial mode due to sampling, the time difference error range can be obtained as followed:

$$t_{i\_\min}^0 - t_{ei} - \frac{2}{f_s} \le \Delta t_i^{0l} \le t_{i\_\max}^0 - t_{si} + \frac{2}{f_s} \tag{19}$$

Substituting $f_s$ =1MHz and let

$$\boldsymbol{T}_{\min}^{0l} = [t_{i\_\min}^0 - t_{ei} - 2]_{1\times N}(1 \le i \le N) \tag{20}$$

$$\boldsymbol{T}_{\max}^{0l} = [t_{i\_\max}^0 - t_{si} + 2]_{1\times N}(1 \le i \le N) \tag{21}$$

where $\boldsymbol{T}_{\min}^{0l}$ and $\boldsymbol{T}_{\max}^{0l}$ are the lower and upper limit matrices of the fluctuation of the modulus time difference, respectively. Using the above matrices to matrix and varialize the equation (19), the time error constraint of the model is as follows:

$$\boldsymbol{T}_{\min}^{0l} \le \Delta \boldsymbol{T}^{0l*} \le \Delta \boldsymbol{T}_{\max}^{0l} \tag{22}$$

If the error between the measured modulus time difference and the ideal modulus time difference is ignored, it is only

possible to obtain the same value as the measured time at the actual fault point, and the objective function (23) is constructed accordingly.

$$\min(e_{sum}) = \min\left(\sum_{i}^{N} \frac{\left|\Delta t_i^{0l} - \Delta t_i^{0l*}\right|}{\Delta t_i^{0l}}\right) \tag{23}$$

The final fault location model obtained is as follows.

$$\begin{cases} \min\left(\sum_{i}^{N} \frac{\left|\Delta t_i^{0l} - \Delta t_i^{0l*}\right|}{\Delta t_i^{0l}}\right) \\ \text{s.t.} \begin{cases} \boldsymbol{V}^{0l*} \cdot \Delta \boldsymbol{T}^{0l*} = \boldsymbol{L}_f \\ \boldsymbol{T}^0_{\min} \le \Delta \boldsymbol{T}^{0l*} \le \boldsymbol{T}^0_{\max} \\ \left|\boldsymbol{V}^{0l} - \boldsymbol{V}^{0l*}\right| \le \dfrac{\varepsilon \times \boldsymbol{L}_f}{\Delta \boldsymbol{T}^{0l}} \end{cases} \end{cases} \tag{24}$$

### C. FAULT LOCATION PROCESS

In this paper, particle swarm optimization (PSO) [30] is used to solve the fault location results. PSO is a swarm intelligence optimization algorithm that can find the optimal solution through cooperation and information sharing among individuals in the group. Due to the existence of equality constraints, it is sufficient to set the distance and time variables to calculate the wave velocity.

#### 1) ABNORMAL DATA IDENTIFICATION AND PROCESSING

When there is obvious abnormal data, there may be cases where the model cannot converge to a smaller value no matter how the particle position changes. This is a consequence of the inconsistency between the time constraint and the wave velocity constraint introduced by the abnormal data. It can be judged by the values of the penalty factors. There are two possibilities for abnormal data that do not meet the constraints: greater than the upper limit or less than the lower limit, which means that the values of penalty factors are non-zero.

#### 2) ACCURATE FAULT LOCATION PROCESS

The specific process of the fault location method based on the modulus time difference is shown in Fig.7.

(1) Collect traveling wave signal data to form a dynamic wave velocity value range.

(2) Identify the faulty line according to the state of the circuit breaker, and mark the node numbers at both ends of the faulty line as A and B, where A<B.

(3) According to the data collected by the wave head, the arrival time and fluctuation range of the aerial mode is extracted.

(4) According to the wave head calibration method of the preferred frequency band, the zero-mode arrival time and fluctuation range and eliminate invalid data is extracted.

(5) Substitute the obtained effective parameters into the established PSO model to solve the fault location results.

(6) If there is no solution, identify abnormal data according to the penalty item.

(7) Eliminate invalid data.

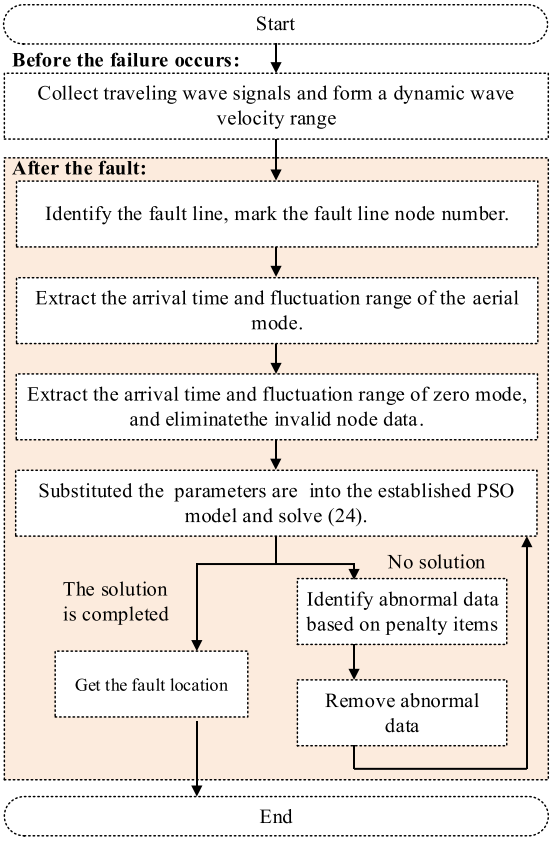


**FIGURE 7.** Flow chart of the method operation.

(8) Repeat step (5) to obtain the fault location result.

## IV. SIMULATION RESULTS AND DISCUSSIONS

### A. SIMULATION MODEL

To verify the accuracy of the proposed fault location method, a distribution network simulation model, as shown in Fig.8 was built by PSCAD/EMTDC. This model is a 10 kV multi-outlet and multi-branch radial distribution network composed of 4 feeders, the longest of which is the main feed line. The system uses a mix of cables and overhead lines, the parameters of the overhead line and cable are indicated in Table 1. In Fig.8, T is the main transformer of the distribution system, and its ratio is 110 kV/10.5 kV. Each branch termination is connected to a Dyn transformer, with a 10 kV/0.4 kV ratio. The loads operate at a constant frequency with 200 kW active power and 40 kvar reactive power. The traveling wave detection devices are installed as shown in Fig.8 to collect traveling wave signals.

### B. SIMULATION ANALYSIS

Set a short-circuit grounding fault in A-B phase 6 km away from node G on line F-G. The interphase resistance is usually small, and is set to be 1 Ω. The ground resistance is 50 Ω. After eliminating the invalid data, the result obtained by inputting valid data into the fault location model is 6.0177 km, with an error of 17.7 m. At this time, the calculated objective

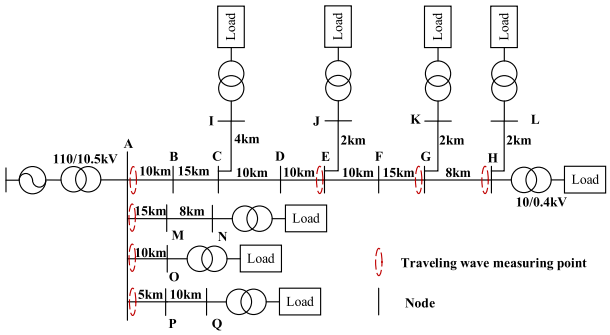


**FIGURE 8.** Topology of the fault simulation model.

**TABLE 1.** Parameters of Medium-voltage overhead lines.

| | | | |
|---|---|---|---|
| positive-sequence parameter | $R_1$ (Ω/km) | $L_1$ (mH/km) | $C_1$ (μF/km) |
| | 0.17 | 1.20 | 0.010 |
| zero-sequence parameter | $R_0$ (Ω/km) | $L_0$ (mH/km) | $C_0$ (μF/km) |
| | 0.23 | 5.48 | 0.008 |

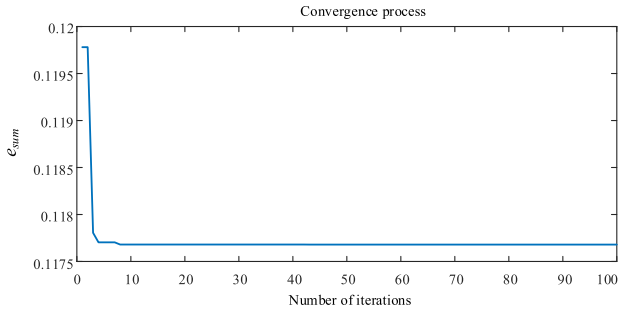


**FIGURE 9.** Convergence process of model.

function is 0.11768. The convergence process is shown in Fig.9. The algorithm can quickly converge to the vicinity of the fault point within 10 iterations and gradually approach the fault point.

The particle distribution of the 95th iteration is shown in Fig.10. The particles are randomly distributed at the initial stage, and some particles cannot meet the wave velocity constraint and time constraint at the same time, so the corresponding objective function is affected by the penalty function, which is much higher than the normal value. However, due to the heuristic optimization characteristics of PSO, the particles quickly gather near the fault point that meets the wave velocity constraint and time constraint at the same time and constantly search for the optimal point. In the feasible domain, as the particle distance parameter approaches the fault distance represented by the modulus time difference information, the value of the objective function gradually shrinks and finally reaches the minimum.

In order to verify the recognition effect of the algorithm on abnormal data, a data error of 1 ms was set at node H, and the model was re-run. The iterative process is depicted in Fig.11

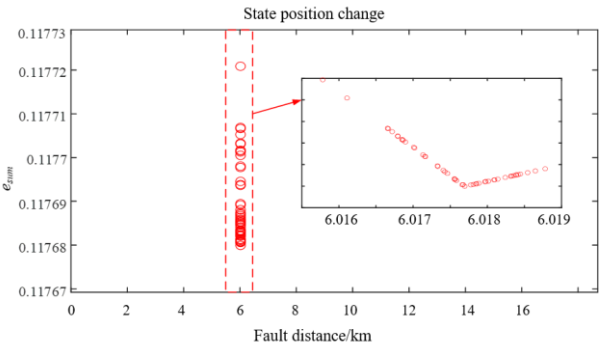


**FIGURE 10.** The distribution of particles in the 95th iteration.

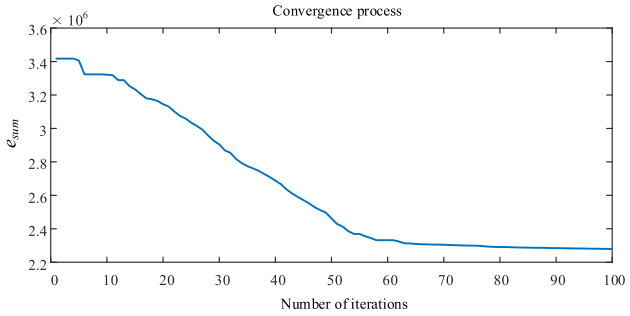


**FIGURE 11.** Convergence process of model when there is abnormal data.

at this time. As can be seen, the value of the objective function still decreases with the number of operations in the algorithm. However, its value decreases slowly, and its minimum value is still high until the end of the iteration, which means that the abnormal data causes a conflict between the time constraint and the wave speed constraint.

The particle distribution of the 95th iteration is shown in Fig.12. Although the model can still get the approximate fault location, the penalty function always plays a role because the constraint contradiction model cannot find a feasible solution that fully complies with the relative wave velocity, modulus time difference inequality constraints. In the end, the objective function can only be maintained at a higher order of magnitude. In this case, the difference between the relative wave velocity and the constrained upper and lower limit $D_{i\_max}$ and $D_{i\_min}$ are shown in Fig.13.

When $D_{i\_max} < 0$ and $D_{i\_min} > 0$, node $i$ can satisfy the wave speed constraint. $D_{G\_max}$ and $D_{G\_min}$ of node H are both less than zero, indicating that the relative wave velocity is limited to a value range less than the lower limit of relative wave velocity due to excessive time error, which is consistent with the setting situation. Therefore, the abnormal data can be identified, and the complete model is rerun after deleting it. The calculated result is 6.0224 km, with an error of 22.4 m. It can be seen that the proposed algorithm can effectively identify the abnormal data collected by each node and locate the fault point after eliminating the abnormal data.

A two-phase ground fault is set between nodes E and F in the simulation model of Fig.8, 25 km away from node G. The

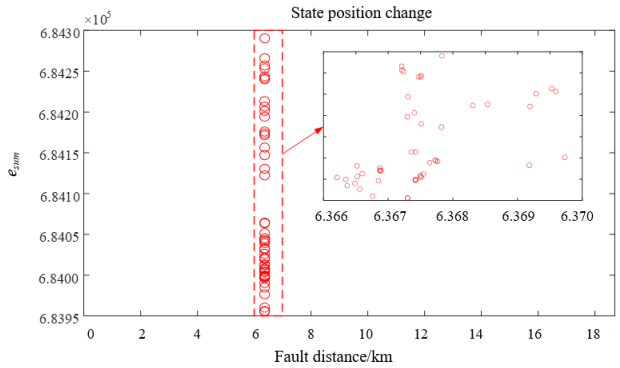


**FIGURE 12.** The distribution of particles in the 95th iteration.

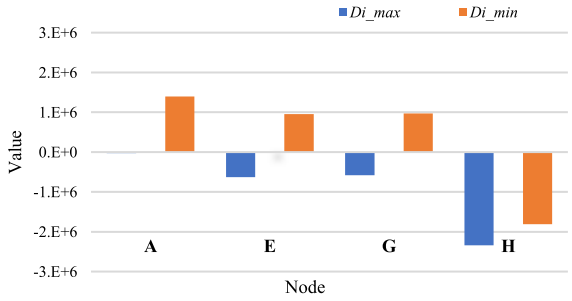


**FIGURE 13.** The value of *Di_max*, *Di_min* when there is abnormal data.

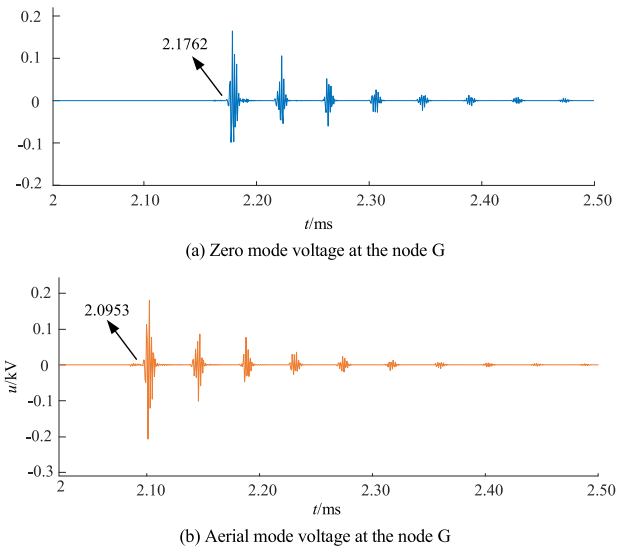


**FIGURE 14.** Traveling wave signal processed by wavelet transform.

traveling wave signal is measured at node E, the transition resistance is set to 50 Ω, and the zero-mode and aerial-mode voltages after the transformation processing by db6 wavelet are shown in Fig.14.

According to Fig.14, there is a certain difference in the arrival time of the aerial mode and the zero mode of the fault traveling wave in the power distribution system, so the method based on the modulus time difference is feasible in the power distribution system. From Fig.14 (a) and (b), we know

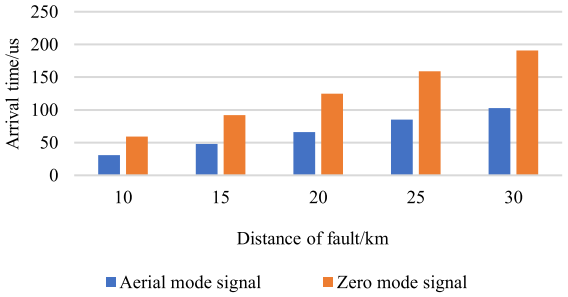


**FIGURE 15.** Arrival time of traveling wave head.

**TABLE 2.** Results of different fault locations.

| No. | Faulty line | Fault distance/km | Fault location error/km |
|---|---|---|---|
| 1 | Node A-B | 5 | 0.0132 |
| 2 | Node B-C | 10 | 0.0145 |
| 3 | Node C-D | 5 | 0.0245 |
| 4 | Node D-E | 5 | 0.0191 |
| 5 | Node E-F | 5 | 0.0272 |
| 6 | Node F-G | 5 | 0.0218 |
| 7 | Node F-G | 10 | 0.0173 |
| 8 | Node A-M | 10 | 0.0178 |

the arrival time of the first wave of the zero-mode and aerial-mode components at node G is 2.1762 ms and 2.0953 ms, respectively. Based on the time difference between the wave heads of zero mode and aerial mode to reach node G, combined with the propagation speed of two on different lines, it is possible to determine the approximate location of the fault point, then eliminate the pseudo-fault point and precisely locate the fault point.

In order to further verify the extraction effect of the proposed method on the arrival time of the mode component wave heads, two-phase ground faults were set at different positions upstream node G on the main feeder line. The fault resistance was 50 Ω, and the traveling wave signals were acquired at node G. The results were shown in Fig.15. The fault location in the figure refers to the distance from node G.

As the traveling wave transmission distance increases, the difference between the arrival times of the two modulus wave heads becomes more and more obvious. In addition, the arrival time of the traveling wave head is not absolutely proportional to the fault distance, but with the increase of the fault distance, the arrival time of the traveling wave head will become longer, which is consistent with the theoretical analysis of wave speed attenuation in Section II.

To verify the location effect of the proposed method at different fault locations, two-phase ground faults are set at different locations of the grid with a time error of 1-2$\mu$s. The results are shown in Table 2. The simulation results show that the proposed method can locate faults on different lines at different distances, and the error is less than 30 m.

To verify whether the accuracy of this method meets the requirements for new energy access, two nodes K and N in the model shown in Fig.8 are connected with 50 kW photovoltaics, and the fault location is performed again.

**TABLE 3.** Results under distributed generator access.

| No. | Faulty line | Fault distance/km | Fault location error/km |
|---|---|---|---|
| 1 | Node A-B | 5 | 0.0141 |
| 2 | Node B-C | 10 | 0.0164 |
| 3 | Node E-F | 5 | 0.0327 |
| 4 | Node F-G | 5 | 0.0232 |
| 5 | Node F-G | 10 | 0.0194 |
| 6 | Node A-M | 10 | 0.0191 |
| 7 | Node A-B | 5 | 0.0157 |
| 8 | Node A-M | 10 | 0.0279 |

**TABLE 4.** Results under different grounding resistances.

| No. | Grounding resistance/Ω | Fault distance/km | Fault location error/km |
|---|---|---|---|
| 1 | 100 | 5 | 0.0223 |
| 2 | 200 | 5 | 0.0242 |
| 3 | 200 | 10 | 0.0182 |
| 4 | 400 | 10 | 0.0175 |

**TABLE 5.** Results in case of abnormal data.

| No. | Time synchronization error | Abnormal location | Abnormal location recognition results | Fault location error/km |
|---|---|---|---|---|
| 1 | 0.1ms | E | E | 0.0136 |
| 2 | 0.1ms | H | H | 0.0153 |
| 3 | 0.1ms | E、H | E、H | 0.0196 |
| 4 | 1ms | E | E | 0.0148 |
| 5 | 1ms | H | H | 0.0175 |
| 6 | 1ms | E、H | E、H | 0.0232 |

In addition, to test the applicability of the proposed method for single-phase grounding faults, two sets of single-phase ground faults (No.7 and No.8) are set up. The results are shown in Table 3.

It can be clearly observed that under the influence of new energy and power electronic equipment access, the arrival time of the traveling wave head has a slight change, but the result can still be guaranteed to be within 35 m, which has little impact on the overall fault location accuracy. Therefore, this method can be applied to the fault location of the distribution network with the new energy access, including single-phase ground fault.

The following section examines the fault location accuracy of this method for various grounding resistances. Set a two-phase grounding fault on the line between nodes F and G with different rounding resistances. When grounding faults occur in distribution networks, the type of grounding medium is complex and may include various high-impedance grounding environments, such as soil, gravel, grassland, concrete, branches, pits, and tiles [31]. In addition, the resistance is also affected by temperature and humidity. Considering the influence of various factors, the maximum resistance selected is 400 Ω. Table 4 displays the results. The error of fault location can still be kept within an acceptable range, indicating that the method is less impacted by grounding resistance and has strong resistance to transition resistance.

Based on the simulation in Section IVB, abnormal data of different locations and proportions were set on the main feeder line. The results are shown in Table 5.

**TABLE 6.** Comparison results with several methods.

| Methods | Wave velocity attenuation | Abnormal data | Synchronization | Location error |
|---|---|---|---|---|
| [21] | Not considered | Not considered | Yes | 29.6 m |
| [32] | Not considered | Not considered | Yes | 22.6 m |
| Proposed method | Considered | Considered | No | 20.1 m |

Simulation results show that the proposed method can recognize and process abnormal data, and ensure that the fault location error is less than 0.1%.

### C. COMPARED WITH OTHER METHODS

1∼2 $\mu$s random error was set on the faults of cases 2, 5, and 7 in Table 2, and the fault location comparison results with other methods are shown in Table 6.

Fault location in [21] is performed by setting virtual fault points to calculate the mismatch degree, but this method does not consider the inconsistency of the whole network due to wave speed attenuation when solving wave velocity. [32] By using the reflection coefficient for fault localization, but ignoring the attenuation of the wave speed, the error is large. In this paper, wave velocity decay is considered, and the penalty function during particle swarm solving is used to indicate and eliminate anomalous data. In addition, the proposed method does not require synchronization, which reduces the cost and difficulty of actual-field practice. Under the condition of the same sampling rate and 10$\mu$s synchronization accuracy, the location error of the proposed method is less than 20.1 m, which has higher location accuracy than [21] and [32].

## V. CONCLUSION

1) The amplitude attenuation and frequency dependent wave speed in the process of traveling wave transmission are analyzed, and the inconsistent characteristics of the whole network caused by wave speed attenuation are summarized. The time-frequency characteristics of zero-mode traveling wave are analyzed, and a wave head calibration method considering background noise is proposed according to the characteristics of time-frequency noise in whole time domain.

2) By analyzing the proportional relationship between the modulus time difference and the fault distance through analysis, we define the relative wave velocity and establish the constraint on the modulus time difference, relative wave velocity, and transmission distance. In addition, a location model is established with the weighted deviation of the modulus time difference as the objective function and realized by PSO algorithm, and the abnormal data are identified according to the penalty term.

3) After connecting to the distribution network, distributed generators and power electronic equipment will produce a large number of harmonics, and selecting the proper fault traveling wave frequency band will effectively reduce the effects of higher harmonics. Before the control system is activated, the fault features are only affected by the network

topology and its parameters, and not by the control strategy. As a result, the fault location method based on the initial traveling wave head has good adaptability.

4) A 10 kV multi-branch radiation distribution network model was built by PSCAD/EMTDC, and case analysis, wave head arrival time analysis, and abnormal data analysis were carried out for the proposed method. The results demonstrate that the proposed method has advantages in terms of fault location accuracy and time synchronization.

## REFERENCES


[1] R. Li, W. Wang, and M. Xia, "Cooperative planning of active distribution system with renewable energy sources and energy storage systems," *IEEE Access*, vol. 6, pp. 5916–5926, 2018.

[2] Y. H. Song, H. L. Gao, G. F. Zhu, and B. G. Zhao, "A single-phase matrix algorithm for fault location of two-phase earthing fault in distribution systems," in *Proc. China Int. Conf. Electr. Distribution (CICED)*, Shenzhen, China, Sep. 2014, pp. 1430–1433.

[3] J.-P. Zhou, Y.-P. Zheng, and Z.-P. Wang, "Detection of the transmission line short-circuited fault based on lifting wavelet," in *Proc. 3rd Int. Conf. Electric Utility Deregulation Restructuring Power Technol.*, Nanjing, China, Apr. 2008, pp. 1663–1666.

[4] L.-P. Wu, C. Huang, Y. Qi, W. Zhao, and H.-T. Jiang, "A new adaptive matrix algorithm for fault location in distribution network with distributed generation," in *Proc. Int. Conf. Electr. Control Eng.*, Yichang, China, Sep. 2011, pp. 499–504.

[5] R. H. Salim, M. Resener, A. D. Filomena, K. R. Caino de Oliveira, and A. S. Bretas, "Extended fault-location formulation for power distribution systems," *IEEE Trans. Power Del.*, vol. 24, no. 2, pp. 508–516, Apr. 2009.

[6] A. Dubey, H. Sun, D. Nikovski, J. Zhang, T. Takano, Y. Kojima, and T. Ohno, "Locating of multi-phase faults of ungrounded distribution system," in *Proc. Int. Conf. Power Syst. Technol.*, Chengdu, China, Oct. 2014, pp. 1657–1664.

[7] J. Wei, S. Xiao, and W. Dong, "Fault location method for active distribution network based on SVM and feature search algorithm," in *Proc. IEEE 3rd Int. Electr. Energy Conf. (CIEEC)*, Beijing, China, Sep. 2019, pp. 66–71.

[8] F. Coffele, C. Booth, and A. Dysko, "An adaptive overcurrent protection scheme for distribution networks," *IEEE Trans. Power Del.*, vol. 30, no. 2, pp. 561–568, Apr. 2015.

[9] K.-H. Chao, S.-H. Ho, and M.-H. Wang, "Modeling and fault diagnosis of a photovoltaic system," *Electr. Power Syst. Res.*, vol. 78, no. 1, pp. 97–105, Jan. 2008.

[10] J. U. N. de Nunes and A. S. Bretas, "Extended impedance-based fault location formulation for active distribution systems," in *Proc. IEEE Power Energy Soc. Gen. Meeting (PESGM)*, Boston, MA, USA, Jul. 2016, pp. 1–5.

[11] K. Yu, J. Zeng, X. Zeng, F. Xu, Y. Ye, and Y. Ni, "A novel traveling wave fault location method for transmission network based on directed tree model and linear fitting," *IEEE Access*, vol. 8, pp. 122610–122625, 2020.

[12] S. Shi, B. Zhu, A. Lei, and X. Dong, "Fault location for radial distribution network via topology and reclosure-generating traveling waves," *IEEE Trans. Smart Grid*, vol. 10, no. 6, pp. 6404–6413, Nov. 2019.

[13] L. Xie, L. Luo, Y. Li, Y. Zhang, and Y. Cao, "A traveling wave-based fault location method employing VMD-TEO for distribution network," *IEEE Trans. Power Del.*, vol. 35, no. 4, pp. 1987–1998, Aug. 2020.

[14] R. J. Hamidi and H. Livani, "A recursive method for traveling-wave arrival-time detection in power systems," *IEEE Trans. Power Del.*, vol. 34, no. 2, pp. 710–719, Apr. 2019.

[15] F. V. Lopes and E. J. S. Leite, "Traveling wave-based solutions for transmission line two-terminal data time synchronization," *IEEE Trans. Power Del.*, vol. 33, no. 6, pp. 3240–3241, Dec. 2018.

[16] F. V. Lopes, K. M. Dantas, K. M. Silva, and F. B. Costa, "Accurate two-terminal transmission line fault location using traveling waves," *IEEE Trans. Power Del.*, vol. 33, no. 2, pp. 873–880, Apr. 2018.

[17] F. V. Lopes, P. Lima, J. P. G. Ribeiro, T. R. Honorato, K. M. Silva, E. J. S. Leite, W. L. A. Neves, and G. Rocha, "Practical methodology for two-terminal traveling wave-based fault location eliminating the need for line parameters and time synchronization," *IEEE Trans. Power Del.*, vol. 34, no. 6, pp. 2123–2134, Dec. 2019.

[18] S. Zhang, G. Zou, Q. Huang, and H. Gao, "A traveling-wave-based fault location scheme for MMC-based multi-terminal DC grids," *Energies*, vol. 11, no. 2, p. 401, Feb. 2018.

[19] M. Korkali, H. Lev-Ari, and A. Abur, "Traveling-wave-based fault-location technique for transmission grids via wide-area synchronized voltage measurements," *IEEE Trans. Power Syst.*, vol. 27, no. 2, pp. 1003–1011, May 2012.

[20] Y. Chen, D. Liu, and B. Xu, "Wide-area traveling wave fault location system based on IEC61850," *IEEE Trans. Smart Grid*, vol. 4, no. 2, pp. 1207–1215, Jun. 2013.

[21] R. Liang, F. Wang, G. Fu, X. Xue, and R. Zhou, "A general fault location method in complex power grid based on wide-area traveling wave data acquisition," *Int. J. Electr. Power Energy Syst.*, vol. 83, pp. 213–218, Dec. 2016.

[22] Q. Zhao, Z. Wang, and Y. Wang, "Fault location method for an active distribution network based on a hierarchical optimization model and fault confidence factors," *Electronics*, vol. 12, no. 6, p. 1314, Mar. 2023.

[23] G. Liang, P. Liyuan, L. Ruihuan, Z. Fen, and W. Xin, "Fault location in distribution network with distributed generation based on neural network," in *Proc. China Int. Conf. Electr. Distribution (CICED)*, Shenzhen, China, Sep. 2014, pp. 209–212.

[24] M. Gil, A. A. Abdoos, and M. Sanaye-Pasand, "A precise analytical method for fault location in double-circuit transmission lines," *Int. J. Electr. Power Energy Syst.*, vol. 126, Mar. 2021, Art. no. 106568.

[25] H. W. Dommel, *Electromagnetic Transients Program Rule Book*. Portland, OR, USA: Bonneville Power Administration, 1982.

[26] N. Peng, K. Ye, R. Liang, T. Hou, G. Wang, X. Chen, and S. Teng, "Single-phase-to-earth faulty feeder detection in power distribution network based on amplitude ratio of zero-mode transients," *IEEE Access*, vol. 7, pp. 117678–117691, 2019.

[27] L. Jiang, Q. Chen, W. Huang, Y. Zeng, L. Wang, and P. Zhao, "A novel directional pilot protection method for VSC-MTDC based on the initial forward and backward travelling wave head," *Int. J. Electr. Power Energy Syst.*, vol. 109, pp. 198–206, Jul. 2019.

[28] J. Ding, X. Wang, Y. Zheng, and L. Li, "Distributed traveling-wave-based fault-location algorithm embedded in multiterminal transmission lines," *IEEE Trans. Power Del.*, vol. 33, no. 6, pp. 3045–3054, Dec. 2018.

[29] J.-J. Jiang, W.-X. Wei, W.-L. Shao, Y.-F. Liang, and Y.-Y. Qu, "Research on large-scale bi-level particle swarm optimization algorithm," *IEEE Access*, vol. 9, pp. 56364–56375, 2021.

[30] S. Hong, B. Wang, and X. Liu, "Transmission line traveling wave fault location based on empirical mode decomposition de-noising," in *Proc. Int. Conf. Electr., Electron. Mechatronics*, Phuket, Thailand, 2015, pp. 30–33.

[31] X. Lin, H. Chen, K. Xu, and J. Xu, "Time estimation algorithm of single-phase-to-ground fault based on two-step dimensionality reduction," *Energies*, vol. 16, no. 13, p. 4921, Jun. 2023.

[32] S. Robson, A. Haddad, and H. Griffiths, "Traveling wave fault location using layer peeling," *Energies*, vol. 12, no. 1, p. 126, Dec. 2018.


**XIAOFENG REN** received the B.S. degree in power system automation from Southeast University, Nanjing, China, in 2002, and the M.S. degree in management from Soochow University, Suzhou, China, in 2011. He is currently pursuing the Ph.D. degree in electrical engineering with the China University of Mining and Technology. He is also with State Grid Xuzhou Power Supply Company, Xuzhou, China. He severs as the Chief of the Party Committee of the Company. His current research interest includes modern power system operation.

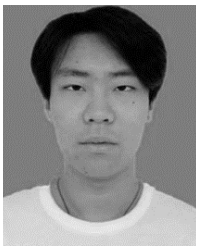

**YIHANG PAN** received the B.S. degree in electrical engineering from the China University of Mining and Technology, Xuzhou, China, in 2022, where he is currently pursuing the M.S. degree in electrical engineering. His main research interests include fault location and power system protection.

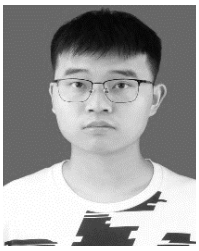

**MENG HOU** received the B.S. degree in electrical engineering from the China University of Mining and Technology, Xuzhou, China, in 2022, where he is currently pursuing the M.S. degree in electrical engineering. His main research interests include fault location and power system protection.

**RUI LIANG** (Senior Member, IEEE) received the B.Sc. and Ph.D. degrees from the Department of Electrical Engineering, China University of Mining and Technology, in 2001 and 2010, respectively. Since 2001, he has been with the China University of Mining and Technology, where he is currently the Deputy Director of the Jiangsu Province Laboratory of Electric and Automation. He has been awarded 30 patents and published two books and over 60 conference and journal publications. His current research interests include protection in power grid, critical electrical equipment assessment, and modeling in energy interconnection.

**LINGDONG SU** received the B.S. degree in power system automation from the Nanjing University of Information Science and Technology, Nanjing, China, in 2008, the M.S. degree from the Jiangsu University of Science and Technology, Zhenjiang, China, in 2011, and the Ph.D. degree from North China Electric Power University, in 2016. His current research interests include power system control and electrical information technology.

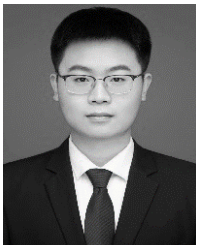

**QUANJIN WANG** received the B.S. degree in electrical engineering from the Qingdao University of Science and Technology, Qingdao, China, in 2020, and the M.S. degree from the China University of Mining and Technology, Xuzhou, China, in 2023. He is currently with State Grid Linyi Power Supply Company, Linyi, China. His main research interests include traveling wave fault location and power system protection.

**PENG ZHANG** (Graduate Student Member, IEEE) received the B.Eng. and M.Sc. degrees from the School of Electrical and Electronic Engineering, Shandong University of Technology, Zibo, China, in 2017 and 2020, respectively. He is currently pursuing the Ph.D. degree with the China University of Mining and Technology, Xuzhou, China. His current research interests include incipient fault identification and the detection of distribution networks.